ACTA MECHANICA SOLIDA SINICA 30 (2017) 374–389

Available online at www.sciencedirect.com

ScienceDirect

journal homepage: www.elsevier.com/locate/CAMSS

# A 3D multi-field element for simulating the electromechanical coupling behavior of dielectric elastomers

*Jun Liu*, Choon Chiang Foo, Zhi-Qian Zhang*

*Institute of High Performance Computing, A*STAR, 1 Fusionopolis Way, #16-16 Connexis, 138632, Singapore*

ARTICLE INFO

*Article history:*
Received 4 April 2017
Revised 27 June 2017
Accepted 7 July 2017
Available online 8 August 2017

*Keywords:*
Dielectric elastomer
Electromechanical coupling
Implicit multi-field finite element method
Eigenvalue problem

ABSTRACT

We propose a multi-field implicit finite element method for analyzing the electromechanical behavior of dielectric elastomers. This method is based on a four-field variational principle, which includes displacement and electric potential for the electromechanical coupling analysis, and additional independent fields to address the incompressible constraint of the hyperelastic material. Linearization of the variational form and finite element discretization are adopted for the numerical implementation. A general FEM program framework is developed using C++ based on the open-source finite element library deal.II to implement this proposed algorithm. Numerical examples demonstrate the accuracy, convergence properties, mesh-independence properties, and scalability of this method. We also use the method for eigenvalue analysis of a dielectric elastomer actuator subject to electromechanical loadings. Our finite element implementation is available as an online supplementary material.



## 1. Introduction

Dielectric elastomers (DE) are a class of electroactive polymers, which have attracted immense attention in recent years due to their ability to achieve extremely large deformation under an electric field. Subject to a voltage, a DE membrane thins down and expands in its in-plane directions. Extremely large in-plane expansions, exceeding several hundred percent strains, have been observed in experiments [1–4]. This capability to achieve large voltage-actuated strains has motivated intense developments in an emerging field of soft machines [5,6], which include actuators [4,7–9], sensors [10], and power generators [11,12].

In some applications, the dielectric elastomer is actuated at high frequencies and used as resonators [13–17], duct silencers [18], pumps [19], and loudspeakers [3]. Consequently, the dielectric elastomer undergoes nonlinear oscillation and displays a rich interplay of complex behavior. By adjusting pre-stretch or loading conditions, the natural frequency of DE may be modified, which allows the natural frequency to be tuned [13,20,21]. Actuated by a sinusoidal voltage, the dielectric elastomer may exhibit resonance at multiple excitation frequencies [13,20,22]. Current work on the dynamic response of dielectric elastomers is largely based on experiments [17,19,23] and theoretical models for simple configurations [13,16,20,22,24]. However, numerical studies based on simulation tools are very limited.

* Corresponding author.
*E-mail addresses:* nickliujun@gmail.com, liuj@ihpc.a-star.edu.sg (J. Liu).

http://dx.doi.org/10.1016/j.camss.2017.07.005
0894-9166/

To design practical DE transducers for the aforementioned applications, recent efforts have focused on developing simulation tools capable of predicting the electromechanical response of dielectric elastomers, which may undergo large and inhomogeneous deformation. Most simulation methods are based on a nonlinear finite-deformation field theory of dielectric elastomers; and a recent review is available in [25]. One common approach is to implement the constitutive models for these materials in commercial finite element software, where ABAQUS has emerged as a popular choice. In ABAQUS, user-defined material models (UMAT) can be defined to incorporate the electromechanical coupling through the free energy density of the material, without introducing additional field nodal variables [26–28]. However, because this simplified method cannot be used to analyze complex devices such as dielectric elastomer generators and electromechanical instability (EMI), user-defined element in ABAQUS (UEL) has been developed for this scenario [29,30]. Similarly, in-house codes have also been developed by various groups to study phenomena such as electromechanical actuation, instabilities, and viscoelasticity. Zhou et al. [31] used a meshless method to investigate the propagation of wrinkles in dielectric elastomers. Zhang et al. [32] proposed a semi-explicit method to simulate the snap-through instability for dielectric elastomers; however, explicit time integration schemes require small time step and may not be optimal for quasi-static problems, and explicit method cannot be used for eigenvalue analysis. Park et al. [33–36] developed an implicit finite element model for elastic and viscoelastic dielectric elastomers based on the Sandia-developed simulation code Tahoe [37]. More recently, Schlogl and Leyendecker [38] implemented a viscoelastic DE model based on the deal.II library [39]; and Ortigosa et al. [40] developed a computational framework based on multi-variable strain energies. Generally, these in-house source codes are not available to the community.

In this paper, we present an implicit finite element method based on the nonlinear field theory for dielectric elastomers by Suo [25]. Based on a four-field variational approach, we develop a hybrid element technique that accounts for electromechanical coupling and incompressible behavior for the dielectric elastomer. In finite element modeling of incompressible materials, volumetric locking is a well-known problem. Previous approaches used to address volumetric locking in dielectric elastomers include the F-bar method [29], and the B-bar method [41]. Generally, these two methods can well solve the locking problem and have been widely adopted. However, in the current study, we adopt a multi-field hybrid element to overcome the difficulty. Although it is still inconclusive which methods are superior, we note that the hybrid element technique is available for incompressible materials in ABAQUS standard library and is widely used in industrial applications. It is also not trivial to develop such numerical techniques to simulate the fully coupled electromechanical response of dielectric elastomers with incompressible material behavior. Besides methodology development, we study convergence and stiffness matrix convex properties, parallel computing scalability, and tunable vibration modes of a DE membrane.

The remainder of the paper is organized as follows. Section 2 summarizes the constitutive model for dielectric elastomers. In Section 3, we propose a four-field variational principle and describe the numerical implementation in a general FEM program framework, which is based on the open-source finite element library deal.II [39]. In Section 4, numerical solutions are presented to validate the accuracy, convergence properties, mesh-independence properties, and scalability of this method. We demonstrate the capability of the method to extract the natural frequencies of dielectric elastomer subject to electromechanical loadings in eigenvalue analysis, as well as to conduct implicit dynamics simulation within the current numerical framework by a balloon inflation test.

## 2. Constitutive model for DE

In this section, we begin by summarizing the governing equations used to model the electromechanical response of dielectric elastomers, and then present specific constitutive equations for dielectric elastomers.

### 2.1. *Kinematic description*

Consider a continuum solid body which occupies a spatial domain in the region $\Omega_0$ as the *reference (material)* configuration, where $\boldsymbol{n}_0$ denotes the outward unit normal on the boundary $\partial\Omega_0$ of $\Omega_0$. When deformed, the body occupies a region $\Omega$ in the *current (spatial)* configuration, and $\boldsymbol{n}$ denotes the outward unit normal on the boundary $\partial\Omega$ of $\Omega$. Let $\boldsymbol{X}$ be the coordinates of material particles in the reference state, while $\boldsymbol{x}$ is the corresponding coordinate in the current state, the motion of the body can be described by $\boldsymbol{x}=\chi(\boldsymbol{X},t)$. Throughout this work, tensor notation $\nabla_X(),\nabla_X\bullet()$ and $\nabla_X\times()$ are used to represent the gradient, divergence, and curl of variable in the material configuration, while $\nabla_x(),\nabla_x\bullet()$ and $\nabla_x\times()$ are used to denote the corresponding spatial operations. For two tensors $\boldsymbol{A}$ and $\boldsymbol{B}$ with any order, the operations $\boldsymbol{A}\bullet\boldsymbol{B}$ and $\boldsymbol{A}:\boldsymbol{B}$ are used to represent the single contraction and double contraction operations, respectively.

According to the point-to-point mapping in continuum mechanics, the deformation gradient can be represented in tensor form $\boldsymbol{F}=\nabla_X\boldsymbol{x}$, or $F_{iI}=\frac{\partial x_i}{\partial X_I}$ using index notation, with $J=\det(\boldsymbol{F})$ being the Jacobian of the deformation gradient. The left Cauchy–Green tensor $\boldsymbol{B}$ and right Cauchy–Green tensor $\boldsymbol{C}$ are represented as

$$\begin{aligned}\boldsymbol{B}&=\boldsymbol{F}\cdot\boldsymbol{F}^T \quad \text{or} \quad B_{ij}=F_{ik}F_{jk}\\ \boldsymbol{C}&=\boldsymbol{F}^T\cdot\boldsymbol{F} \quad \text{or} \quad C_{ij}=F_{ki}F_{kj}.\end{aligned} \tag{1}$$

For the most part in our current presentation, we use the tensor notation, and include indicial notation in some places to improve clarity.

### 2.2. *Electrostatics equations*

In the reference configuration, the electric field and the electric displacement are denoted as $\tilde{\boldsymbol{E}}$ and $\tilde{\boldsymbol{D}}$, respectively. According to Maxwell–Faraday equation, in the absence of magnetic fields, the electric field defined on the material configuration

has zero curl:

$$\nabla_X \times \tilde{\boldsymbol{E}} = \boldsymbol{0} \tag{2}$$

which enables us to define an electric potential $\phi$ as

$$\tilde{\boldsymbol{E}} = -\nabla_X \phi. \tag{3}$$

According to Gauss's Law, without the existence of free charge, we have

$$\nabla_X \cdot \tilde{\boldsymbol{D}} = 0. \tag{4}$$

In the current configuration, the electric field $\boldsymbol{E}$ and electric displacement $\boldsymbol{D}$ can be related by the deformation gradient as [25]:

$$\tilde{\boldsymbol{E}} = \boldsymbol{F}^T \cdot \boldsymbol{E} \quad \text{and} \quad \tilde{\boldsymbol{D}} = J\boldsymbol{F}^{-1} \cdot \boldsymbol{D}. \tag{5}$$

### 2.3. *Constitutive equations*

Define the nominal density of the Helmholtz free energy of dielectric as $\Psi(\boldsymbol{F}, \tilde{\boldsymbol{E}})$. Assuming isothermal processes, the variation of free energy density function can be represented as [25]:

$$\delta\Psi = P_{ij}\delta F_{ij} - \tilde{D}_k \delta \tilde{E}_k \tag{6}$$

where the first Piola–Kirchhoff (PK1) stress $P_{ij}$ is work-conjugate to the deformation gradient $\delta F_{ij}$, and the electric displacement $\tilde{D}_k$ is work-conjugate to the electric field $\tilde{E}_k$. Subsequently we can write:

$$P_{ij} = \frac{\partial \Psi\left(\boldsymbol{F}, \tilde{\boldsymbol{E}}\right)}{\partial F_{ij}}, \quad \tilde{D}_k = \frac{\partial \Psi\left(\boldsymbol{F}, \tilde{\boldsymbol{E}}\right)}{\partial \tilde{E}_k}. \tag{7}$$

Therefore, the constitutive equations can be determined by prescribing an appropriate free energy density. In this work, we adopt the model of ideal dielectric elastomers, in which the free energy density function may be expressed as

$$\Psi = \Psi^{\text{mech}} + \Psi^{\text{ele}} \tag{8}$$

which is a sum of free energy components due to mechanical stretching and electrical polarization. For the free energy due to mechanical stretching, we adopt the Gent hyperelastic model [42]:

$$\Psi^{\text{mech}} = \Psi^{\text{dev}}(\bar{\boldsymbol{B}}) + \Psi^{\text{vol}}(J) \tag{9}$$

where $\bar{\boldsymbol{B}}$ is the modified left Cauchy–Green tensor with $\bar{\boldsymbol{B}} = J^{-2/3}\boldsymbol{B}$ and $\det(\bar{\boldsymbol{B}}) = 1$. $\Psi^{\text{dev}}$ and $\Psi^{\text{vol}}$ are the deviatoric and volumetric parts of free energy, respectively

$$\Psi^{\text{dev}} = -\frac{\mu J_m}{2}\ln\left(1 - \left(\bar{I}_1 - 3\right)/J_m\right), \quad \Psi^{\text{vol}} = \frac{K}{2}\left(\frac{J^2-1}{2} - \ln J\right) \tag{10}$$

where $\bar{I}_1$ is the first invariant of $\bar{\boldsymbol{B}}$ as $\bar{I}_1 = tr(\bar{\boldsymbol{B}})$. $\mu$ and $K$ are shear modulus and bulk modulus, respectively. $J_m$ represents the effect of limiting chain extensibility of polymeric molecules. In the model of ideal dielectric elastomers, we assume that the true electric displacement $\boldsymbol{D}$ is linear in the true electric field $\boldsymbol{E}$ [25] as

$$\boldsymbol{D} = \varepsilon \boldsymbol{E} \rightarrow \tilde{\boldsymbol{D}} = J\varepsilon \boldsymbol{C}^{-1} \cdot \tilde{\boldsymbol{E}} \tag{11}$$

where $\varepsilon$ is the permittivity, a material constant independent of deformation. The free energy due to electrical polarization may be expressed as

$$\Psi^{ele} = -\frac{1}{2}J\varepsilon \tilde{\boldsymbol{E}} \cdot \tilde{\boldsymbol{C}}^{-1}\tilde{\boldsymbol{E}}. \tag{12}$$

Hence, the Cauchy stress may be expressed as

$$\boldsymbol{\sigma} = \boldsymbol{\sigma}^{\text{dev}} + \boldsymbol{\sigma}^{\text{vol}} + \boldsymbol{\sigma}^{\text{ele}} \tag{13}$$

where

$$\begin{aligned} \boldsymbol{\sigma}^{\text{dev}} &= \frac{\mu}{J}\left(\frac{\bar{\boldsymbol{B}} - \left(\bar{I}_1/3\right)\boldsymbol{I}}{1 - \left(\bar{I}_1 - 3\right)/J_m}\right) \\ \boldsymbol{\sigma}^{\text{vol}} &= p\boldsymbol{I} = \frac{\partial \Psi}{\partial J}\boldsymbol{I} = \frac{K}{2}\left(J - \frac{1}{J}\right)\boldsymbol{I} \\ \boldsymbol{\sigma}^{\text{ele}} &= \varepsilon\left(\boldsymbol{E} \otimes \boldsymbol{E} - \frac{1}{2}\boldsymbol{I}(\boldsymbol{E} \cdot \boldsymbol{E})\right) \end{aligned} \tag{14}$$

## 3. Four-field variational principle and linearization

### 3.1. *Four-field variational principle*

We present a four-field variational principle that incorporates the displacement field $\boldsymbol{u}$, electric potential field $\phi$, and two additional independent variables $\tilde{p}$ and $\tilde{J}$ which are used to impose the incompressibility constraint in dielectric elastomers. $\tilde{J}$ is a kinematic variable which serves as a constraint on the dilational deformation $J$ enforced by the Lagrange multiplier $\tilde{p}$, as shown in Eq. (15). Following the Simo–Taylor–Pister variation principle in [43], we denote the field variable space as $\boldsymbol{\Xi} \equiv (\boldsymbol{u}, \phi, \tilde{p}, \tilde{J})$, and express the internal and external potentials as

$$\begin{aligned} \Pi^{\text{int}}(\boldsymbol{\Xi}) &= \int_{\Omega_0} \left\{\Psi^{\text{dev}}(\bar{\boldsymbol{C}}(\boldsymbol{u})) + \Psi^{\text{vol}}\left(\tilde{J}\right) + \tilde{p}\left[J(\boldsymbol{u}) - \tilde{J}\right] + \Psi^{\text{ele}}(\boldsymbol{u}, \phi, J(\boldsymbol{u}))\right\} dV \\ \Pi^{\text{ext}}(\boldsymbol{u}, \phi) &= \int_{\Omega_0} \boldsymbol{b}_0^p \cdot \boldsymbol{u} dV + \int_{\partial\Omega_0} \boldsymbol{t}_0^p \cdot \boldsymbol{u} dA - \int_{\partial\Omega_0} \omega_0^p \phi dA \end{aligned} \tag{15}$$

where $\bar{\boldsymbol{C}}$ is the modified right Cauchy–Green tensor with $\bar{\boldsymbol{C}} = J^{-2/3}\boldsymbol{C}$ and $\det(\bar{\boldsymbol{C}}) = 1$. $\boldsymbol{b}_0^p$ and $\boldsymbol{t}_0^p$ are prescribed body force and surface traction respectively in the reference configuration. $\omega_0^p$ is the prescribed surface charge density in the reference configuration. For our simulations, we neglect volumetric free charge. According to variational principle, the system is in equilibrium when

$$\delta\left(\Pi^{\text{int}} - \Pi^{\text{ext}}\right) = 0 \tag{16}$$

The variation of internal potential $\delta\Pi^{\text{int}}(\Xi)$ can be derived as follows:

$$\begin{aligned}\delta\Pi(\Xi) &= D_{\delta u}\Pi(\Xi) + D_{\delta\phi}\Pi(\Xi) + D_{\delta\tilde{p}}\Pi(\Xi) + D_{\delta\tilde{J}}\Pi(\Xi)\\ &= \int_{\Omega_0} \delta \boldsymbol{e} : \left[\boldsymbol{S}^{\text{dev}} + J(\boldsymbol{u})\tilde{p}\boldsymbol{C}^{-1} + \boldsymbol{S}^{\text{ele}}\right] dV\\ &\quad + \int_{\Omega_0} \left(\tilde{\boldsymbol{D}} \cdot \nabla_X \delta\phi\right) dV + \int_{\Omega_0} \left\{\delta\tilde{p}\left[J(\boldsymbol{u}) - \tilde{J}\right]\right\} dV\\ &\quad + \int_{\Omega_0} \left\{\delta\tilde{J}\left[\frac{\partial \Psi^{\text{vol}}\left(\tilde{J}\right)}{\partial \tilde{J}} - \tilde{p}\right]\right\} dV \end{aligned} \tag{17}$$

where $\boldsymbol{e}$ is the Green strain measure. $\boldsymbol{S}^{\text{dev}}$ is the deviatoric part of second Piola–Kirchhoff (PK2) stress (in material configuration), and $\boldsymbol{S}^{\text{ele}}$ is the stress contribution of electric field in the material configuration. By imposing an independent pressure-like field, the volumetric stress is now changed to $\boldsymbol{\sigma}^{\text{vol}} = \tilde{p}\boldsymbol{I}$ instead of $\boldsymbol{\sigma}^{\text{vol}} = p\boldsymbol{I}$. Substituting Eqs. (14) and (16) into (15) and writing in separate form, one has

$$\begin{cases} \displaystyle\int_{\Omega_0} \left\{\delta \boldsymbol{e} : \left[\boldsymbol{S}^{\text{dev}} + J(\boldsymbol{u})\tilde{p}\boldsymbol{C}^{-1} + \boldsymbol{S}^{\text{ele}}\right]\right\} dV = \int_{\Omega_0} \boldsymbol{b}^p \cdot \delta\boldsymbol{u} dV + \int_{\partial\Omega_0} \boldsymbol{t}^p \cdot \delta\boldsymbol{u} dA \\ \displaystyle\int_{\Omega_0} \left(\tilde{\boldsymbol{D}} \cdot \nabla_X \delta\phi\right) dV = -\int_{\partial\Omega_0} \omega^p \delta\phi dA \\ \displaystyle\int_{\Omega_0} \left\{\delta\tilde{p}\left[J(\boldsymbol{u}) - \tilde{J}\right]\right\} dV = 0 \\ \displaystyle\int_{\Omega_0} \left\{\delta\tilde{J}\left[\frac{\partial \Psi^{\text{vol}}\left(\tilde{J}\right)}{\partial \tilde{J}} - \tilde{p}\right]\right\} dV = 0 \end{cases} \tag{18}$$

with the Dirichlet boundary conditions as

$$\begin{aligned} \boldsymbol{u}|_{\partial\Omega^{d,u}} &= \boldsymbol{u}^p \\ \phi|_{\partial\Omega^{d,\phi}} &= \phi^p \end{aligned} \tag{19}$$

where $\partial\Omega^{d,u}$ and $\partial\Omega^{d,\phi}$ are the Dirichlet boundaries for displacement and electric potential, respectively; $\boldsymbol{u}^p$ and $\phi^p$ are prescribed displacement and electric potential values on the corresponding Dirichlet boundaries.

### 3.2. *Linearization and finite element implementation*

Eq. (18) is the weak form of the problem and constitutes the governing equations for the electromechanical behavior of the dielectric elastomer. For simplicity, we assume that the force term is invariant within time step, and express Eq. (18) as

$$R(\Xi) = P(\Xi) - Q = 0 \tag{20}$$

where $R$ is the residuals, $P$ is the non-linear equations, and $Q$ is the external force term. Since it is a nonlinear problem, an iterative Newton–Raphson method can be used for solving each non-linear time step. For each time step, assuming $\Xi \equiv (\boldsymbol{u}, \phi, \tilde{p}, \tilde{J})$ has already been solved at iteration $n$, and is denoted as $\Xi^n$, the residual $R$ at iteration $n+1$ can be expanded as

$$R\left(\Xi^{n+1}\right) = R(\Xi^n) + D^2_{\delta\Xi,\Delta\Xi}(\Pi(\Xi^n)) \cdot \Delta\Xi = 0. \tag{21}$$

Therefore, the increment of solution $\Delta\Xi$ can be solved by

$$D^2_{\delta\Xi,\Delta\Xi}(\Pi(\Xi^n)) \cdot \Delta\Xi = -R(\Xi^n) = Q - P(\Xi^n). \tag{22}$$

Detailed form of $D^2_{\delta\Xi,\Delta\Xi}(\Pi(\Xi^n))$ is given as follows:

$$\begin{aligned} D^2_{\delta u,\Delta u}\Pi(\Xi) &= \int_\Omega \frac{\partial \delta u_i}{\partial x_j}\left(\delta_{ik}\sigma_{jl} + \mathfrak{C}_{ijkl}\right)\frac{\partial \Delta u_k}{\partial x_l} dv \\ D^2_{\delta u,\Delta\phi}\Pi(\Xi) &= -\varepsilon\int_\Omega \left\{\frac{\partial \delta u_i}{\partial x_j}\left(\delta_{ik}E_j + \delta_{jk}E_i - \delta_{ij}E_k\right)\frac{\partial \Delta\phi}{\partial x_k}\right\} dv \\ D^2_{\delta\phi,\Delta\phi}\Pi(\Xi) &= -\int_\Omega \left(\frac{\partial \delta\phi}{\partial x_i}\varepsilon\delta_{ij}\frac{\partial \Delta\phi}{\partial x_j}\right) dv \\ D^2_{\delta u,\Delta\tilde{p}}\Pi(\Xi) &= \int_\Omega \left(\frac{\partial \delta u_i}{\partial x_j}\delta_{ij}\Delta\tilde{p}\right) dv \\ D^2_{\delta\tilde{p},\Delta\tilde{J}}\Pi(\Xi) &= -\int_\Omega \delta\tilde{p}\Delta\tilde{J} dv \\ D^2_{\delta\tilde{J},\Delta\tilde{J}}\Pi(\Xi) &= -\int_\Omega \delta\tilde{J}\frac{d^2\Psi^{\text{vol}}\left(\tilde{J}\right)}{d\tilde{J}d\tilde{J}}\Delta\tilde{J} dv \end{aligned} \tag{23}$$

where $\mathfrak{C}_{ijkl}$ is the fourth-order elasticity tensor in the spatial description, and the explicit expression can be found in Appendix A.

When applying standard finite element discretization, we choose the element where the interpolation order for $\tilde{p}$ and $\tilde{J}$ is an order lower than that for $\boldsymbol{u}$ and $\phi$, for the consideration of stability. In this work, the U8/E8/P1/J1 element (tri-linear interpolation for both displacement and electric potential fields, and the quantities $\tilde{p}$ and $\tilde{J}$ are constant) is adopted for all simulations. Although this type of element does not satisfy the Ladyzhenskaya–Babuska–Brezzi (LBB) condition, it has been widely used because of its simplicity and good convergence characteristics [44]. Hence, we have the finite element interpolation within one element:

$$\begin{aligned} u_i &= \sum_{I=1}^{n_n} N_i^{u(I)} u_i^{(I)} \qquad \phi = \sum_{I=1}^{n_n} N^{\phi(I)}\phi^{(I)} \\ \tilde{p} &= \sum_{I=1}^{n_n} N^{\tilde{p}(I)}\tilde{p}^{(I)} \qquad \tilde{J} = \sum_{I=1}^{n_n} N^{\tilde{J}(I)}\tilde{J}^{(I)} \end{aligned} \tag{24}$$

where $n_n$ is the node number for one element, and $i$ means the $i$th DOF of displacement field $\boldsymbol{u}$. $N_i^{u(I)}$, $N^{\phi(I)}$, $N^{\tilde{p}(I)}$, $N^{\tilde{J}(I)}$ are shape functions of $u_i$, $\phi$, $\tilde{p}$, $\tilde{J}$ corresponds to node $I$. For the current U8/E8/P1/J1 element, we have

$$N_i^u = N^\phi \quad \text{and} \quad N^{\tilde{p}} = N^{\tilde{J}}. \tag{25}$$

Consequently, the linear system of equations for one single element is given as

$$\begin{bmatrix} \boldsymbol{k}^{uu} & \boldsymbol{k}^{ue} & \boldsymbol{k}^{up} & 0 \\ \boldsymbol{k}^{eu} & k^{ee} & 0 & 0 \\ \boldsymbol{k}^{pu} & 0 & 0 & k^{pJ} \\ 0 & 0 & k^{Jp} & k^{JJ} \end{bmatrix} \begin{bmatrix} \Delta\boldsymbol{u} \\ \Delta\phi \\ \Delta\tilde{p} \\ \Delta\tilde{J} \end{bmatrix} = - \begin{bmatrix} \boldsymbol{R}^u \\ R^e \\ R^p \\ R^J \end{bmatrix} = \begin{bmatrix} \boldsymbol{f}^u \\ f^e \\ f^p \\ f^J \end{bmatrix} \tag{26}$$

where

$$k_{ik}^{uu(AB)} = \int_{\Omega^e} \frac{\partial N^{u(A)}}{\partial x_j}\left(\delta_{ik}\sigma_{jl} + \mathfrak{C}_{ijkl}\right)\frac{\partial N^{u(B)}}{\partial x_l} dv$$

$$k_j^{ue(AB)} = -\int_{\Omega^e}\left\{\frac{\partial N^{u(A)}}{\partial x_i}\varepsilon\left(\delta_{jl}E_i+\delta_{il}E_j-\delta_{ij}E_l\right)\frac{\partial N^{\phi(B)}}{\partial x_l}\right\}dv,$$

$$k^{eu(AB)} = \left[k^{ue(AB)}\right]^T$$

$$k^{ee(AB)} = -\int_{\Omega^e}\left(\frac{\partial N^{u(A)}}{\partial x_i}\varepsilon\delta_{ij}\frac{\partial N^{\phi(B)}}{\partial x_j}\right)dv$$

$$k_i^{up(AB)} = \int_{\Omega^e}\left(\frac{\partial N^{u(A)}}{\partial x_j}\delta_{ij}N^{\tilde{p}(B)}\right)dv,\ k^{pu(AB)} = \left[k^{up(AB)}\right]^T$$

$$k^{pJ(AB)} = -\int_{\Omega^e} N^{\tilde{p}(A)}N^{\tilde{J}(B)}dv,\ k^{Jp(AB)} = k^{pJ(AB)}$$

$$k^{JJ(AB)} = \int_{\Omega} N^{\tilde{J}(A)}\frac{d^2\Psi^{vol}\left(\tilde{J}\right)}{d\tilde{J}d\tilde{J}}N^{\tilde{J}(B)}dv \tag{27}$$

$k_{ik}^{uu(AB)}$ represents the matrix entry corresponding to the ith DOF of node A and kth DOF of node B related to the displacement part; and this representation applies to all the rest submatrices. $\int_{\Omega^e} dv$ is the integration within the spatial element domain.

The RHS of Eq. (26) has the form

$$\begin{bmatrix} f^u \\ f^e \\ f^p \\ f^J \end{bmatrix} = \begin{bmatrix} \int_{\Omega^e} N^u b_i^p dv + \int_{\partial\Omega^e} N^u t_i^p da - -\int_{\Omega^e}\sigma_{ij}\frac{\partial N^u}{\partial x_j}dv \\ -\int_{\partial\Omega^e} N^\phi\omega^p da - -\int_{\Omega^e}\varepsilon E_i\frac{\partial N^\phi}{\partial x_i}dv \\ \int_{\Omega^e}\left(J-\tilde{J}\right)da \\ \int_{\Omega^e}\left(\frac{d\Psi}{d\tilde{J}}-\tilde{p}\right)da \end{bmatrix}. \tag{28}$$

In assembling Eq. (26) into a global tangent stiffness matrix, three methods may be adopted, to arrange the global DOF index. Assuming the hexahedral element with linear interpolation for $\boldsymbol{u}$ and $\phi$, while constant values for $\tilde{p}$ and $\tilde{J}$, we can have the following three arrangement schemes, i.e.

(1) Arrange all the DOFs element-wise, i.e.

$\{\boldsymbol{u}_1, \phi_1, \boldsymbol{u}_2, \phi_2, \ldots\ldots \boldsymbol{u}_8, \phi_8, \tilde{p}_1, \tilde{J}_1\}, \ldots\ldots \{\boldsymbol{u}_{ndof-7}, \phi_{ndof-7}, \ldots\ldots \boldsymbol{u}_{ndof}, \phi_{ndof}, \tilde{p}_{nele}, \tilde{J}_{nele}\}$, where *ndof* is the number of DOFs in the system, and *nele* is the number of elements in the system.

For this method, the global stiffness matrix will be globally sparse, hence no special treatment is required, and the linear system equations can be solved directly. This method is logically simplest and easiest to implement. However, since the existence of $\tilde{p}$ and $\tilde{J}$ terms will increase the band-width of the sparse matrix, a much longer solution time may be required. Moreover, if an iterative solver is adopted, it is very difficult to find an effective pre-conditioner for this complicated coupling system.

(1) Arrange all the DOFs component-wise, i.e.

$$\{\boldsymbol{u}_1, \boldsymbol{u}_2, \ldots \boldsymbol{u}_{nnode}\},\ \{\phi_1, \phi_2, \ldots \phi_{nnode}\},\ \{\tilde{p}_1, \tilde{p}_2, \ldots \tilde{p}_{nele}\},\ \left\{\tilde{J}_1, \tilde{J}_2, \ldots \tilde{J}_{ele}\right\}.$$

The resulting global stiffness matrix for this scheme is a block-wise sparse matrix, and has a structure similar to the element stiffness matrix in Eq. (26). In order to solve this, we need to condense $\tilde{p}$ and $\tilde{J}$ terms from the global stiffness matrix first, and then solve a block sparse matrix as the structure of

$$\begin{bmatrix} K^{uu} & K^{ue} \\ K^{eu} & K^{ee} \end{bmatrix}\begin{bmatrix} \Delta\boldsymbol{u} \\ \Delta\phi \end{bmatrix} = \begin{bmatrix} f^u \\ f^e \end{bmatrix}. \tag{29}$$

Because this stiffness matrix is block sparse with a full bandwidth, some special techniques are required for effectively solving this linear system. Hence, in this study, we mainly use the third method which is described as follows:

(1) Arrange $\boldsymbol{u}$ and $\phi$ element-wise, while $\tilde{p}$ and $\tilde{J}$ component-wise, i.e.

$$\{\boldsymbol{u}_1, \phi_1, \boldsymbol{u}_2, \phi_2, \ldots \boldsymbol{u}_{nnode}, \phi_{nnode}\},\ \{\tilde{p}_1, \tilde{p}_2, \ldots \tilde{p}_{nele}\}\left\{\tilde{J}_1, \tilde{J}_2 \ldots \tilde{J}_{ele}\right\}.$$

Denoting $\xi \equiv (\boldsymbol{u}, \phi)$, the global stiffness matrix for this scheme is given as

$$\begin{bmatrix} K^{\xi\xi} & K^{\xi p} & 0 \\ K^{p\xi} & 0 & K^{pJ} \\ 0 & K^{Jp} & K^{JJ} \end{bmatrix}. \tag{30}$$

By performing a static condensation technique analogous to that described in [39], the final linear system is reduced to

$$\tilde{K}^{\xi\xi}\Delta\boldsymbol{\xi} = \tilde{f}^{\xi} \tag{31}$$

where

$$\begin{aligned} \tilde{K}^{\xi\xi} &= K^{\xi\xi} + K^{\xi p}\bar{K}K^{p\xi} \\ \tilde{f}^{\xi} &= f^{\xi} - K^{\xi p}\left[\left(K^{Jp}\right)^{-1}f^J - \bar{K}f^p\right] \\ \bar{K} &= \left(K^{Jp}\right)^{-1}K^{JJ}\left(K^{pJ}\right)^{-1}. \end{aligned} \tag{32}$$

Thus, the large-deformation nonlinear electromechanical behavior of dielectric elastomer can be solved with any suitable linear solver. The algorithm proposed in this work is implemented using C++, based on the open-source FEM library deal.II.

## 4. Numerical simulation

In this section, we validate the proposed methodology and show its potential capability. Unless specified otherwise, the material parameters are selected as $\rho = 1000\ \text{kg/m}^3$, $\mu = 4.3\times10^4$ Pa, $K = 4.3\times10^{10}$ Pa, $J_m = 115$, and $\varepsilon = 4.12225\times10^{-11}$ F/m. For a better comparison with the theoretical results, in all the numerical simulation tests, we normalize the voltage and charge as

$$\hat{\phi} = \frac{\phi}{H}\sqrt{\frac{\varepsilon}{\mu}},\quad \hat{Q} = \frac{Q}{L^2\sqrt{\varepsilon\mu}} \tag{33}$$

where $H$ is the original characteristic thickness of the DE sample, and $L$ is the original characteristic length of the sample (i.e. edge length for square and radius for circle).

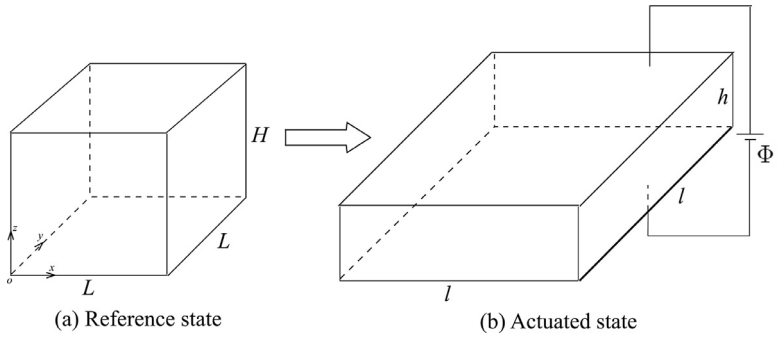


**Fig. 1. – (a) In the reference state, the dielectric elastomer has thickness *H* and lengths *L*. (b) In the actuated state, subject to in-plane force *P* and voltage Φ through the thickness direction, the dielectric elastomer undergoes equal-biaxial deformation and deforms to thickness *h* and lengths *l*.**

### 4.1. *Benchmark test*

We first analyze the equibiaxial deformation behavior of a dielectric elastomer membrane, which is sandwiched between two compliant electrodes. The schematics are shown in Fig. 1. In the reference state, the block has a square cross-section in the *x*–*y* plane, with length *L*, and height *H*. In the actuated state, the block undergoes in-plane expansion, and its original dimensions *L* and *H* respectively become $L'$ and $H'$ without volume change. Therefore, the stretch of the material can be represented as

$$\lambda = L'/L = \sqrt{H/H}' \tag{34}$$

- $u_x = 0$ at the $x = 0$ surface
- $u_y = 0$ at the $y = 0$ surface
- $u_z = 0$ and $\hat{\phi} = 0$ at the $z = 0$ surface

In Fig. 2, we plot the voltage–stretch response curves of the dielectric elastomer under various levels of pre-stretches. The pre-stretch is the stretch at which $\hat{\phi} = 0$. At each pre-stretch $\lambda_{pre}$, the traction force *P* is kept as constant, while charge is applied on the $z = H$ surface. At low pre-stretch, when charge is ramped up initially, the electrical potential increases and the elastomer expands in area. When the charge is sufficiently large, the elastomer thins down appreciably, such that the electric field is high and the voltage needed to maintain the charge starts to decrease. This results in a peak in the voltage–stretch curve and marks the onset of electromechanical instability, which is a well-known phenomenon [45]. Electromechanical stability may be averted by pre-stretching [2], as also seen for the cases when $\lambda_{pre} > 2$. When the elastomer is subject to a large charge, the elastomer undergoes strain-stiffening, and the voltage again increases with charge. Numerical results compare well with theoretical predictions [32] for all cases in Fig. 2.

Dielectric elastomers are generally modeled as incompressible; in finite element simulations, compressible hyperelastic models are often used to avoid numerical difficulties, where the bulk modulus *K* is assumed to be much higher than the shear modulus $\mu$ for simulating a nearly incompressible material behavior. However, a large $K/\mu$ value may cause ill-conditioned stiffness matrix [43], or volumetric locking when fully integrated linear elements are used. We then ask what value of $K/\mu$ is appropriate. For an dielectric elastomer at $\lambda_{pre} = 1$ and $\lambda_{pre} = 6$ with four different values of $K/\mu$, we plot the simulated voltage–stretch plots and compare them with the theoretical results which assume incompressibility, as shown in Fig. 3. When $\lambda < 6.5$, the results are insensitive to the choice of $K/\mu$, implying $K/\mu = 10^3$ may be suitable in most simulation scenarios. However, at very large stretches approaching the extension limit of the elastomer

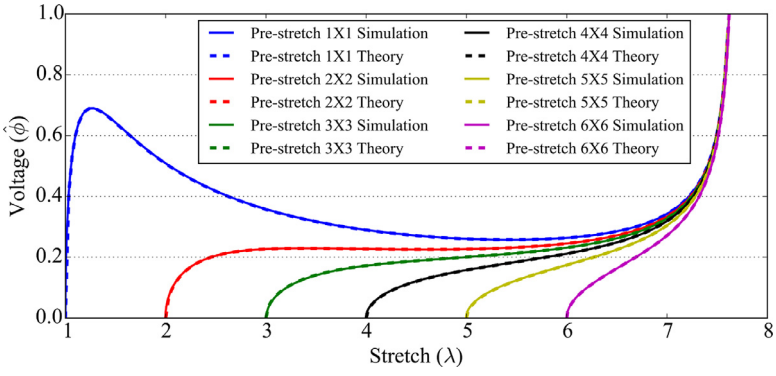


**Fig. 2. – Voltage–stretch curves of the dielectric elastomer under equal-biaxial deformation in a charge-control procedure. The theoretical curves are compared with the simulation results. The value of pre-stretch $\lambda_{pre}$ for each curve can be interpreted from the intersection between the curve and the horizontal axis.**

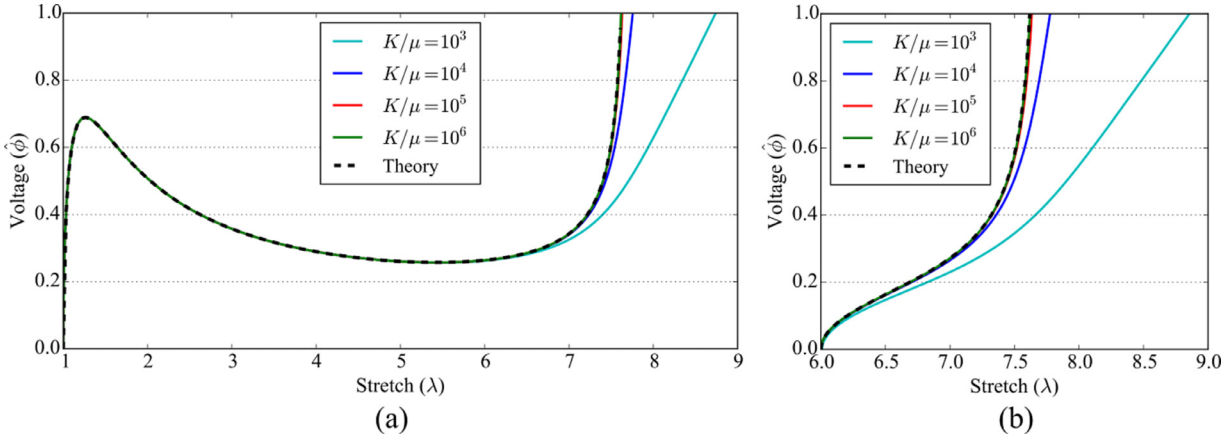


**Fig. 3. – Voltage–stretch plots for various bulk moduli $K$ when (a) $\lambda_{pre}=1$ (b) $\lambda_{pre}=6$.**

where strain-stiffening becomes significant, we find that $K/\mu > 10^4$ would be more suitable.

Next, a convergence study is conducted for the nonlinear solver. The Newton–Raphson method is used to solve the nonlinear equations, and within one nonlinear iteration step, the tangent stiffness matrix for one element is given as

$$\begin{bmatrix} \boldsymbol{k}^{uu} & \boldsymbol{k}^{ue} \\ \boldsymbol{k}^{eu} & k^{ee} \end{bmatrix} \tag{35}$$

which is denoted as the *fully coupled* form. However, in some commercial solver for multiphysics simulation [46,47], when the coupling terms are not easy to be obtained, and the coupling is weak between different fields, we may ignore the coupling term and use

$$\begin{bmatrix} \boldsymbol{k}^{uu} & 0 \\ 0 & k^{ee} \end{bmatrix} \tag{36}$$

to assemble the global stiffness matrix. We call this *weakly coupled* form. Since this is only a Newton–Raphson step, the final solution will not be influenced as long as the non-linear solver converges. The advantage of this form is its simplicity, and it can avoid solving ill-conditioned problems which exist in many multiphysics simulations. A linear solver can solve this equation system much faster than the fully coupled ones. However, the main drawback is the slow convergence when the multiphysics coupling is strong. Here, we investigate the convergence behavior of these two forms. For simplicity, only one non-linear iteration step is simulated, and the prescribed normalized voltage is $\hat{\phi}^p = 0.34$, since above this value the weakly coupled form cannot converge at all. Residuals for voltage and displacement with respect to iteration number are plotted in Fig. 4(a) and (b), respectively. It is clear that the fully coupled form converges much faster than the weakly coupled form. In order to achieve a residual of $10^{-4}$, the fully coupled form requires only 4 iterations, while the weakly coupled form requires at least 10 iterations. The fully coupled form is superior to the weakly coupled form in this case.

Besides the convergence rate, interestingly the coupling term can also aid the convergence of a Newton–Raphson method when electromechanical instability (EMI) occurs. It is known that the free energy of a typical dielectric elastomer material is globally non-convex [25,45]. This property of free energy generally results in a non-positive definite Hessian at EMI, leading to convergence failure when using the Newton–Raphson method. However, by imposing appropriate boundary conditions, such as those in this benchmark test, the free energy shows a local convex property, which enables the implementation of Newton-Raphson method even in the EMI region. A more straightforward way to explain this is rewriting Eq. (29) by separating out the Dirichlet boundary condition, and the global linear system for a fully coupled form can be conceptually represented as

$$\begin{bmatrix} \hat{\boldsymbol{K}}^{uu} & \hat{\boldsymbol{K}}^{ue} & 0 \\ \hat{\boldsymbol{K}}^{eu} & \hat{\boldsymbol{K}}^{ee} & 0 \\ 0 & 0 & \boldsymbol{D}_K \end{bmatrix} \begin{bmatrix} \boldsymbol{u} \\ \phi \\ \boldsymbol{\xi}^p \end{bmatrix} = \begin{bmatrix} \hat{\boldsymbol{f}}^u \\ \hat{\boldsymbol{f}}^e \\ \boldsymbol{f}^p \end{bmatrix} \tag{37}$$

where the hat accent $\wedge$ on the $\boldsymbol{K}$ matrix represents the submatrix term after eliminating the Dirichlet boundary constraint entries, while $\boldsymbol{D}_K$ denotes the corresponding Dirichlet boundary constraint entries. The superscript $p$ represents the prescribed boundary conditions. The submatrices for fully coupled form and weakly coupled form are respectively denoted as

$$\mathrm{S} = \begin{bmatrix} \hat{\boldsymbol{K}}^{uu} & \hat{\boldsymbol{K}}^{ue} \\ \hat{\boldsymbol{K}}^{eu} & \hat{\boldsymbol{K}}^{ee} \end{bmatrix}, \quad \mathrm{S}^w = \begin{bmatrix} \hat{\boldsymbol{K}}^{uu} & 0 \\ 0 & \hat{\boldsymbol{K}}^{ee} \end{bmatrix}. \tag{38}$$

In the simulation of this benchmark, it is found that the determinant of $\mathbf{S}$ matrix is always positive even in the EMI region, i.e. $\det(\mathbf{S}) > 0$. This property ensures the convergence of Newton–Raphson method, so that a minimum free energy can be found. However, without considering the coupling term, it is shown that just before EMI, there is a conversion from $\det(\mathbf{S}^w) > 0$ to $\det(\mathbf{S}^w) < 0$, which prohibits the convergence of Newton–Raphson method from finding a local minimum point of free energy.

In the above discussion regarding the simulation in Fig. 4, the weakly coupled form converges much slower than the fully coupled form, which can be expected because a relatively high voltage is applied in one iteration step. However, if the applied load/voltage rate is limited by some other factors,

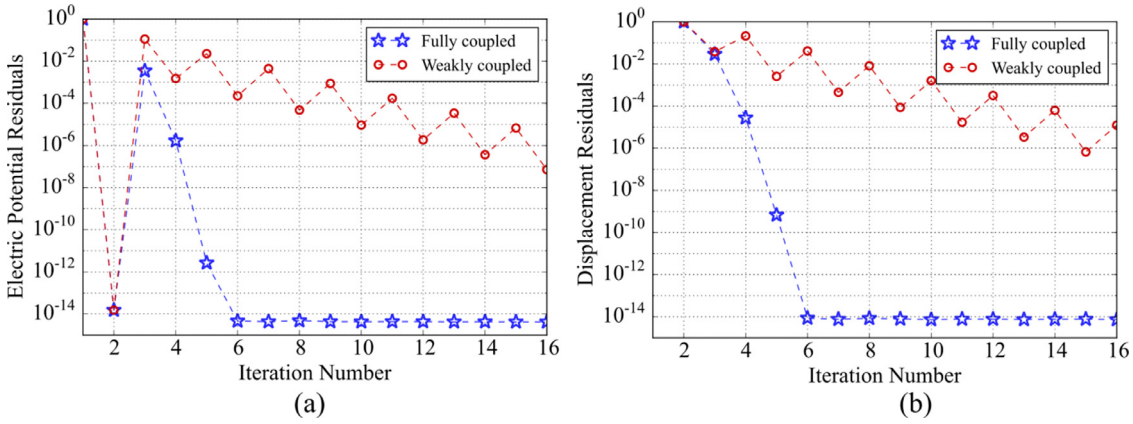


**Fig. 4. – Comparison of convergence rates for (a) voltage and (b) displacement between fully and weakly coupled forms.**

such as time steps and loading rates in a dynamic simulation, the weakly coupled form may exhibit a similar convergence behavior as the fully coupled one. In our experience, both converge within 3 iterations. In this case, the weakly coupled form may have a similar or faster computing time compared to the fully coupled counterpart, since the linear system solver used for the weakly coupled form takes less time in each iteration. Furthermore, this weakly coupled form can only be adopted without the existence of EMI, since the local non-convex property of stiffness matrix prohibits the convergence of a Newton–Raphson method, which limits its application range.

### 4.2. *Bending cantilever*

We next simulate the bending of a cantilever beam, which is made of two parts, as illustrated in Fig. 5(a). The upper part is an elastomer, with length $L$, height $H/2$, and thickness $T$. The lower part is a dielectric elastomer, with the same material properties and dimensions, subject to an applied voltage. Similar 2D cantilever beams have been investigated in [29]. In the current study, we simulate this 2D case by enforcing plane strain boundary conditions on the front and back surfaces of the 3D model. The boundary conditions are given as

- $u_y = 0$ at the $y = 0$ or $y = T$ surface
- $u_x = 0$ at the $x = 0$ surface
- $u_x = u_y = u_z = 0$ along the y-axis
- $\phi = 0$ at the $z = 0$ surface
- $\phi = \phi^p$ at the $z = -H/2$ surface.

As voltage is applied, the lower part of the beam extends due to the incompressible behavior under Maxwell stress, resulting in bending of the beam, as shown in Fig. 5(b). The bending angle $\theta$ is measured with respect to the applied voltage for comparison with the published results in [29]. Fig. 6(a) shows the initial and final cantilever configurations when $\hat{\phi} = 0.5$. Fig. 6(b) illustrates the evolution of bending angle with respect to the applied normalized voltage, the result of which matches the reference result in [29] very well. This simulation shows that our method is capable of handling large rotation problems without encountering the locking problem.

Using this cantilever bending problem, we also investigate the scalability of the proposed model. Computational cost is evaluated for different numbers of DOFs, and the convergence rate to achieving the accurate result is also considered. For the smallest simulation case, we consider only 2 elements along the z direction, and 20 elements distributed in the x direction. Subsequently, all elements are split into 4 sub-elements (with only one single element kept in the y direction), serving as the mesh setup for the next simulation run. In total, seven simulations are performed, which involves 163,840 elements, corresponding to 1321,992 DOFs. As for a benchmark test, $\hat{\phi}^p = 0.05$ is applied to the model within one iteration step, and all the simulations are run on a dual-socket workstation with two Intel Xeon X5650 processors and 32 G RAM. Fig. 7(a) shows the wallclock time per iteration with an increasing number of DOFs. The computational cost scales almost linearly with the number of DOFs.

The solution convergence capability of mesh refinement is also studied, where the bending angle of the beam after

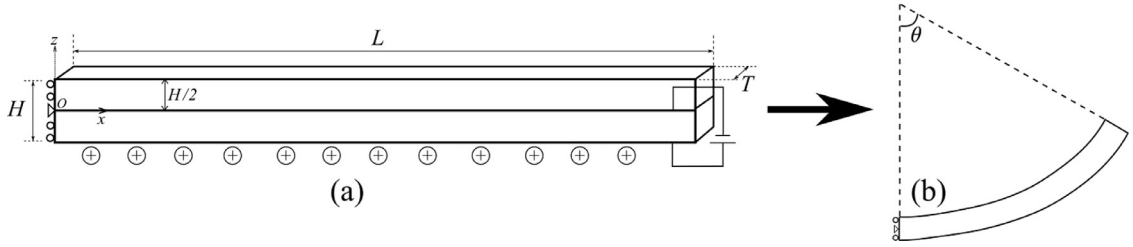


**Fig. 5. – (a) Schematics of a dielectric elastomer bilayer actuator in the reference state. (b) The actuator bends with an angle $\theta$ in response to a voltage applied on its lower half.**

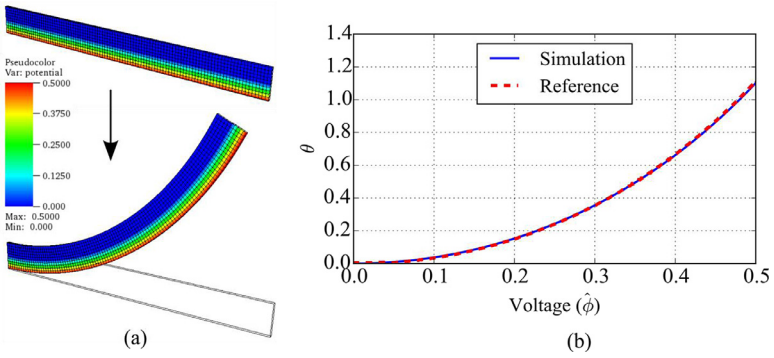


**Fig. 6. – (a) Contour plot of the voltage before and after applying $\hat{\phi} = 0.5$. (b) Bending angle $\theta$ versus applied voltage $\hat{\phi}$ between simulated results and reference results [29].**

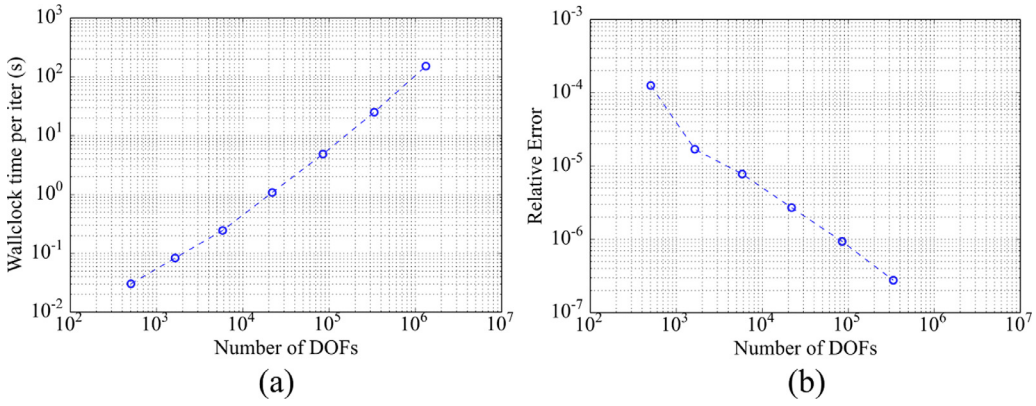


**Fig. 7. – (a) Wallclock time per iteration for different numbers of DOFs. (b) Relative error of bending angle at different numbers of DOFs.**

applying voltage is evaluated. The value of $\theta$ obtained using 163,840 elements is chosen as the reference result, and the relative error is evaluated as

$$e^{\theta} = \frac{\left|\theta - \theta^{\text{ref}}\right|}{\theta^{\text{ref}}}. \tag{39}$$

The convergence of the solution increases monotonically with the number of DOFs, as shown in Fig. 7(b).

With increasing demand of large-scale models, computational time cost is a concern for researchers and software users. In high performance computing, one interest is in the performance of code in a parallelized computing environment, either on shared-memory or distributed-memory machines. For this work, we investigate how a symmetric multiprocessor system (SMP) with shared memory may enhance our algorithm. Within the application of programming with deal.II library, the thread-based parallelization library TBB [48] is adopted to compute the local matrix contribution for assembly, while a direct sparse linear solver UMFPACK [49] can utilize multiple cores to speed up the linear system solution time. A strong scaling problem is investigated here, with two mesh densities considered. Both models are simulated on different numbers of CPU cores up to the maximum capability, i.e. 12, and the wallclock time per iteration is plotted in Fig. 8(a). The speedup ration $S$ and parallel efficiency $E$ are respectively defined as

$$S = \frac{T_1}{T_N} \text{ and } E = \frac{S}{N} \tag{40}$$

where $N$ is the number of cores adopted, $T_1$ is the time cost for serial calculation, and $T_N$ is the time cost when $N$ cores are used for the same problem. Fig. 8(b) shows the speedup ratios of these two models for different CPU cores. Models with different DOFs appear to have a similar and stable scalability. For 2 cores, the parallel efficiency reaches the highest value and nearly linear speedup ratio; while for 12 cores, the program reaches the highest speedup, which is around 6, corresponding to an efficiency of 0.5. This reasonable result demonstrates the parallelization capability of our current model.

### 4.3. *Vibration mode of rectangular membrane without applying electric field*

Phenomena such as coexistent phases [2,45] and nonlinear oscillation [20,22] in dielectric elastomers have elicited interest from the community, and analyses of these phenomena usually involve solving eigenvalue problems in some form. In this section, we focus on vibration of a dielectric elastomer membrane to demonstrate the capability of our method in eigenvalue analysis. By modifying Eq. (31), the governing equation

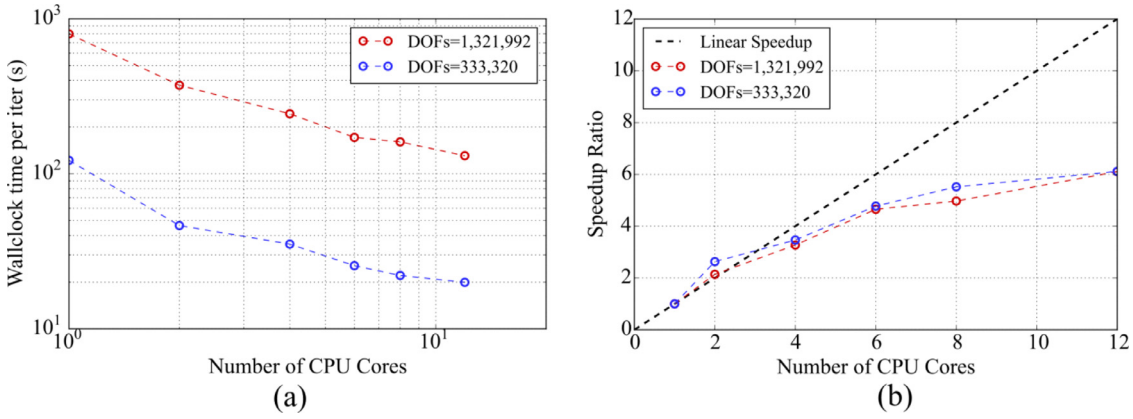


**Fig. 8. – (a) Wallclock time per iteration with large DOFs for different CPU cores. (b) Parallel speedup ratio with large DOFs for different CPU cores.**

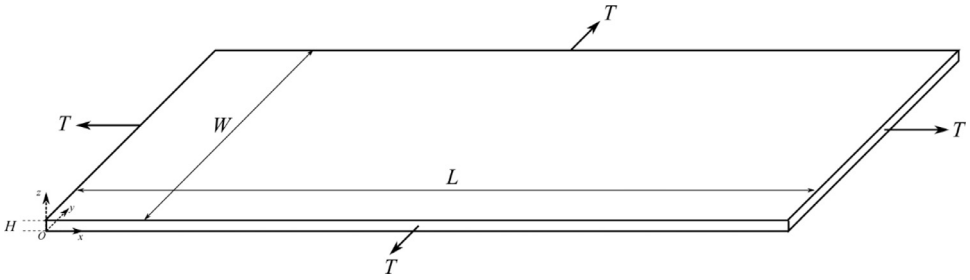


**Fig. 9. – Schematics of rectangular membrane without applied voltage.**

of the dynamic problem can be represented as

$$\mathbf{M}^{\xi\xi}\ddot{\boldsymbol{\xi}} + \tilde{\mathbf{K}}^{\xi\xi}\Delta\boldsymbol{\xi} = \tilde{\mathbf{f}}^{\xi} \tag{41}$$

where $\mathbf{M}^{\xi\xi}$ is the mass matrix coupling the $\boldsymbol{u}$ and $\phi$ terms element-wise. Since there is no inertial effect for the electric potential part, the corresponding term in $\mathbf{M}^{\xi\xi}$ is zero. Hence, we have the element-wise form of the mass matrix:

$$\mathbf{M}^{e^{\xi\xi}} = \begin{bmatrix} \mathbf{M}^{e^{uu}} & 0 \\ 0 & 0 \end{bmatrix} \tag{42}$$

where $\mathbf{M}^{e^{uu}} = \int_{\Omega_0^e} \rho \mathbf{N}^{u^T} \mathbf{N}^u dV$ is the standard element mass matrix.

This approach has previously been adopted in the eigenvalue analysis for piezoelectric materials [50]. Assuming a harmonic solution and solving the homogeneous form of Eq. (41), we have the eigenvalue problem as

$$\left(\tilde{\mathbf{K}}^{\xi\xi} - \omega^2 \mathbf{M}^{\xi\xi}\right)\boldsymbol{\xi} = 0 \tag{43}$$

where $\omega$ is the angular natural frequency, and $\boldsymbol{\xi}$ is the corresponding eigenvector. This equation is solved using the eigenvalue solver provided by Trilinos [51] – a high performance linear algebra library.

Consider a rectangular membrane of dimension $L \times W \times H$, as shown in Fig. 9, where $L = 100$ mm, $W = 50$ mm, and $H = 0.1$ mm. For theoretical analysis, we assume the membrane to be infinite thin, such that the traction $T$ and density $\rho$ is evaluated based on per line and per area, respectively. However, for the 3D finite element model, we simulate this with a very thin brick model, such that $T$ and $\rho$ become the area traction and volume density, respectively. All the boundaries are fixed in all three directions. Analytically, the natural frequency is given as [52]:

$$f = \frac{\omega}{2\pi} = \frac{1}{2}\sqrt{\frac{T}{\rho}}\sqrt{\frac{m^2}{L^2} + \frac{n^2}{W^2}} \tag{44}$$

where $m$ and $n$ are the mode numbers along the length and the width directions, respectively.

Two simulations with different pre-stretch values are conducted, i.e. $\lambda_{\text{pre}} = 2$ and $\lambda_{\text{pre}} = 4$, respectively. For each case, the eigenvalue analysis is performed based on the pre-stretched state. The first 4 frequencies and mode profiles for both simulations are illustrated in Fig. 10, and compared with the theoretical results. Both theoretical and simulation results appear to be in good agreement.

The theoretical and simulation frequencies for the first 10 modes with two different pre-stretches are plotted in Fig. 11, which shows a reasonable agreement between both sets of results. A higher pre-stretch leads to a higher natural frequency. Besides, the frequencies for $\lambda_{\text{pre}} = 4$ are much higher than those for $\lambda_{\text{pre}} = 2$, which is within expectation. Figs. 10 and 11 demonstrate the validity of the current model in solving eigenvalue problems. This capability greatly extends the potential application of this model.

| | | 1st mode | 2nd mode | 3rd mode | 4th mode |
|---|---|---|---|---|---|
| $\lambda_{pre}=2$ | Theory Freq. | 149 Hz | 188 Hz | 240 Hz | 274 Hz |
| | Simulated Freq. | 150 Hz | 189 Hz | 242 Hz | 275 Hz |
| | Mode Plot | 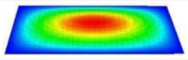 | 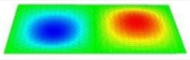 | 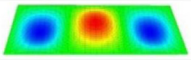 | 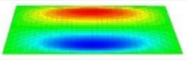 |
| $\lambda_{pre}=4$ | Theory Freq. | 339 Hz | 429 Hz | 546 Hz | 625 Hz |
| | Simulated Freq. | 339 Hz | 429 Hz | 548 Hz | 626 Hz |
| | Mode Plot | 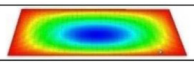 | 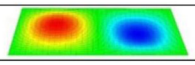 | 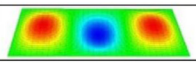 | 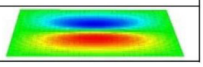 |

**Fig. 10. – Comparison of theoretical and simulation results for rectangular membrane vibration mode and frequency, in the first four modes under different pre-stretches.**

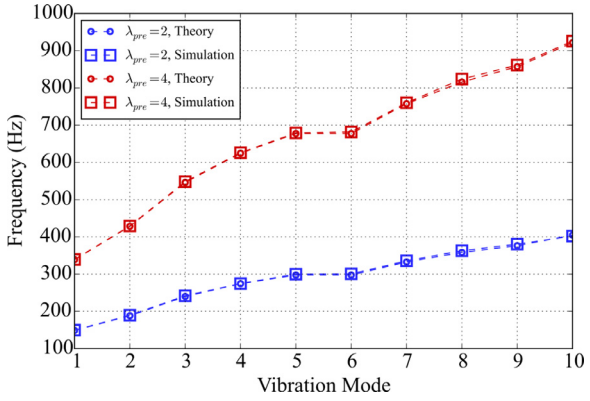


**Fig. 11. – Comparison between theoretical and simulation results for the first 10 frequencies at different pre-stretches.**

### 4.4. *Vibration mode of circular membrane with applying electric field*

Now we consider a circular dielectric elastomer membrane, with radius $R=50$ mm and thickness $H=0.0625$ mm, as shown in Fig. 12. Voltage is applied on a circular region with radius $A$ coated with electrodes at the center of the membrane. Such a configuration has been widely studied experimentally and theoretically [7,18,21]. The natural frequencies and vibration modes under voltage are determined by applying the following boundary conditions:

- $\hat{\phi}=0$ at the $z=0$ surface
- $u_x=u_y=u_z=0$ at $r=\sqrt{x^2+y^2}=R$
- $\hat{\phi}=\hat{\phi}^p$ at the $z=H$ surface with $r\le A$.

After voltage is applied on the pre-stretched membrane ($\lambda_{pre}=1.05$), we solve the eigenvalue problem at the equilibrium state. Fig. 13(a) plots the first four natural frequencies against applied voltage for aspect ratios $R/A=2$ and $R/A=1$. In both cases, the dielectric elastomer is held fixed at its boundary. Under voltage, the active electrode region expands against the surrounding region. Consequently, stresses at the boundaries of the active region decrease with voltage-induced actuation, and the natural frequency also decreases with applied voltage, as shown in Fig. 13(b), which is similar to that observed elsewhere [13,20,21]. At a critical voltage denoted as $\hat{\phi}_c$, the natural frequency vanishes, and the loss of tension occurs.

We also plot the natural frequencies against applied voltage for various pre-stretches in the case of $R/A=1$ in Fig. 14. Our calculations are terminated at the onset of loss of tension. The results show that for all different pre-stretch values, the fundamental frequency has a similar trend with the increasing voltage. The frequency initially decreases relatively slowly for a large range of voltage, and then decreases rapidly within a short range of voltage. Furthermore, it appears that a large pre-stretch allows a higher natural frequency, and by applying an appropriate level of voltage, the dynamics response of the membrane may be actively tuned, as demonstrated in previous studies [21].

To illustrate the change in vibration mode in more detail, we depict the 1st and 4th eigenmodes at the instances when $\hat{\phi}=0$, $\hat{\phi}_m=\hat{\phi}_c/2$, and the critical value $\hat{\phi}_c$ for $R/A=1$ and $R/A=2$. The contours for the vibration mode shapes are shown in Fig. 15.

The 1st eigenmode profile appears similar for both cases of $R/A=1$ and $R/A=2$, when applied voltage is increased from 0 to $\hat{\phi}_m$. However, at the critical voltage $\hat{\phi}_c$, the eigenmode profiles show a discernible difference for both cases. For $R/A=1$, the mode profile is still similar to that of $\hat{\phi}=0$, with only a slight change in the region near the outer boundary. However, for $R/A=2$, all deformation occurs within the region where voltage is applied. This is because the material structural property changes greatly in this region, and becomes much softer compared with the zero electric field region.

Secondly, the situation is slightly different for the 4th eigenmode. The eigenmode profile has already been influenced even when $\hat{\phi}=\hat{\phi}_m$. Besides, when $\hat{\phi}=\hat{\phi}_c$, we can also find that for $R/A=2$, the deformation profile is concentrated within the electrode region. This is similar as that for the 1st eigenmode discussed above.

As a result, some conclusions can be summarized according to this simple simulation. We can find that for the same $R/A$, when applying voltage, higher eigenmode profile patterns are easier to be influenced. With the increase of voltage, this influence gradually affects the lower mode profile patterns. Furthermore, for the same applied voltage, eigenmode profile will be greatly influenced by how the external force/voltage

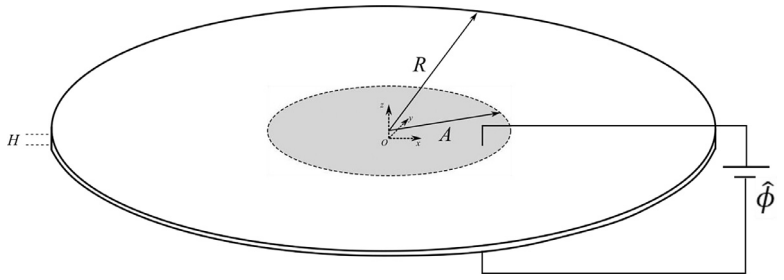


**Fig. 12. – Schematics of a circular dielectric elastomer membrane with electrodes coated on a region of radius A. When voltage is applied, the electrode region expands.**

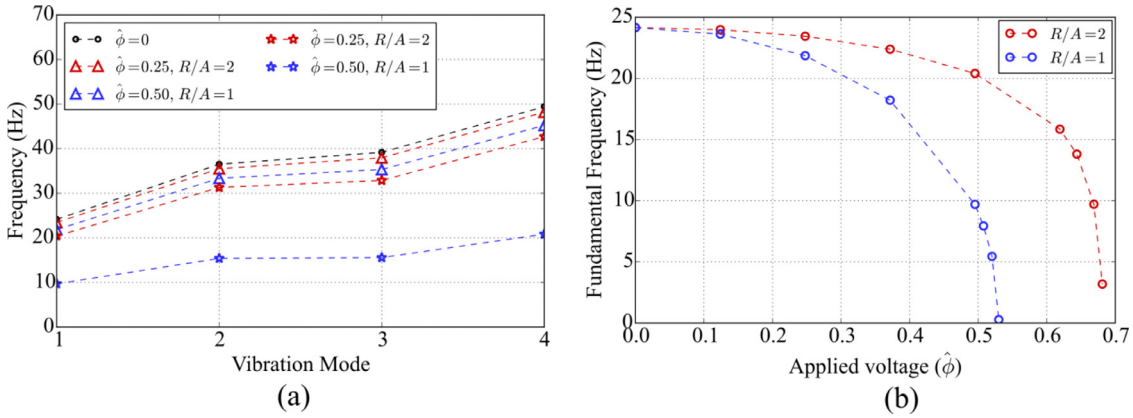


**Fig. 13. – (a) Frequencies in the first four modes for R/A = 2 and R/A = 1 under various applied voltages. (b) Degeneration of membrane stiffness with the increase of applied voltage .**

is applied. Besides, all the simulations show that the applied voltage on membrane softens the structural stiffness, and hence decreases the natural frequency. All these effects can be potentially adopted to a variety of applications because of the capability in frequency turning.

### 4.5. *Dynamic simulation of an inflation balloon*

In the last part, the capability of this model is extended to studying an implicit dynamic problem. Time integration is performed with the Newmark method [44]. Assuming the velocity and displacement at time $t+\Delta t$ have the form

$$\dot{\boldsymbol{u}}^{t+\Delta t} = \dot{\boldsymbol{u}}^{t} + \left[(1-\gamma)\ddot{\boldsymbol{u}}^{t} + \gamma\ddot{\boldsymbol{u}}^{t+\Delta t}\right]\Delta t$$
$$\boldsymbol{u}^{t+\Delta t} = \boldsymbol{u}^{t} + \dot{\boldsymbol{u}}^{t}\Delta t + \left[\left(\frac{1}{2}-\beta\right)\ddot{\boldsymbol{u}}^{t} + \beta\ddot{\boldsymbol{u}}^{t+\Delta t}\right]\Delta t^{2} \tag{45}$$

where $\gamma$ and $\beta$ are Newmark integration parameters, and one typical choice is $\gamma = 1/2$ and $\beta = 1/4$.

Substituting Eq. (45) into Eq. (41) for the dynamic problem (without consideration of damping), we can have the following linear equation system after derivation:

$$\begin{bmatrix} \tilde{\boldsymbol{K}}^{uu} + c_0\boldsymbol{M} & \tilde{\boldsymbol{K}}^{ue} \\ \tilde{\boldsymbol{K}}^{eu} & \tilde{\boldsymbol{K}}^{ee} \end{bmatrix} \begin{bmatrix} \Delta\boldsymbol{u}^{n} \\ \Delta\boldsymbol{\phi}^{n} \end{bmatrix} = \begin{bmatrix} \tilde{\boldsymbol{f}}^{u^n} + \boldsymbol{M}\left[c_0\boldsymbol{u}^{t} - c_0\boldsymbol{u}^{n} + c_2\dot{\boldsymbol{u}}^{t} + c_3\ddot{\boldsymbol{u}}^{t}\right] \\ \tilde{\boldsymbol{f}}^{e^n} \end{bmatrix} \tag{46}$$

where $n$ represents the iteration number in the current time step; $c_0 = 1/(\beta\Delta t^2)$, $c_2 = 1/\beta\Delta t$, and $c_3 = \frac{1}{2\beta} - 1$ are coefficients.

The inflation of a balloon is simulated using the dynamics equations. A schematic of the model and loading procedure is illustrated in Fig. 16. A circular thin membrane of DE is fixed by its edge, and pre-inflated from state (a) to state (b), with an applied excess pressure $p$. Then this pressure is kept constant, and the electric field is applied on the membrane by charge control with a constant ramping rate of $\hat{\omega} = \dot{\omega}t$. During ramping of charge, the membrane undergoes expansion because of the Maxwell stress, and inflates as a balloon. The setup of this

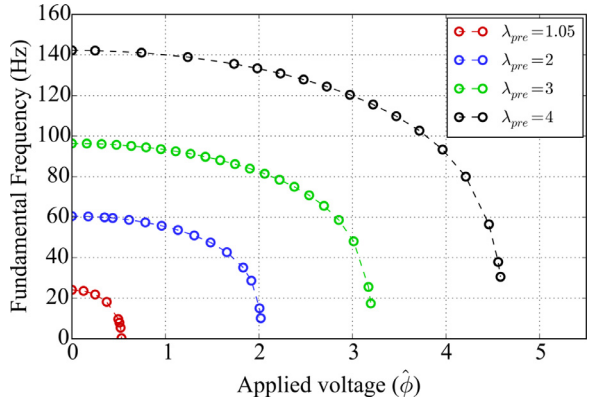


**Fig. 14. – Fundamental frequency is plotted against applied voltage for different pre-stretch setups for the case of R/A = 1.**

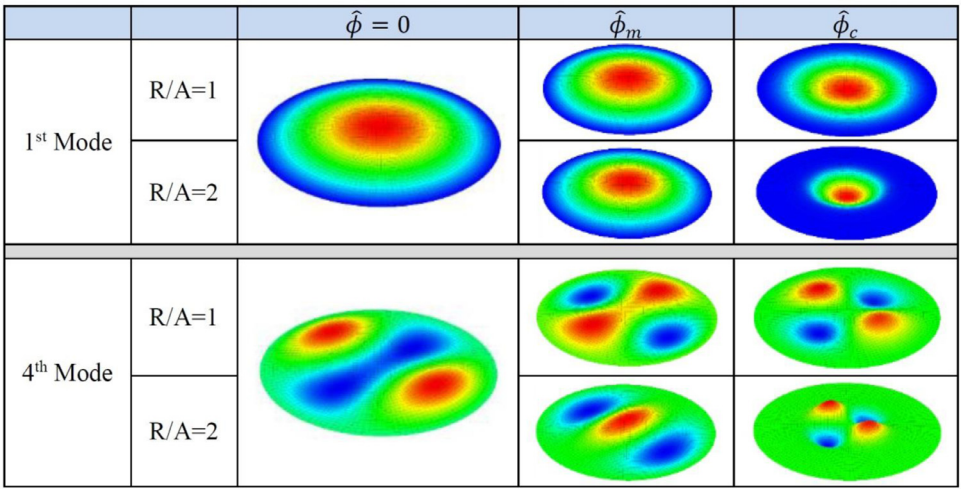


**Fig. 15. – Comparison between vibration modes for R/A = 1 and R/A = 2, at different applied voltages. $\hat{\phi}_m = \hat{\phi}_c/2$, and $\hat{\phi}_c$ represents the critical value of $\hat{\phi}$ during applying voltage.**

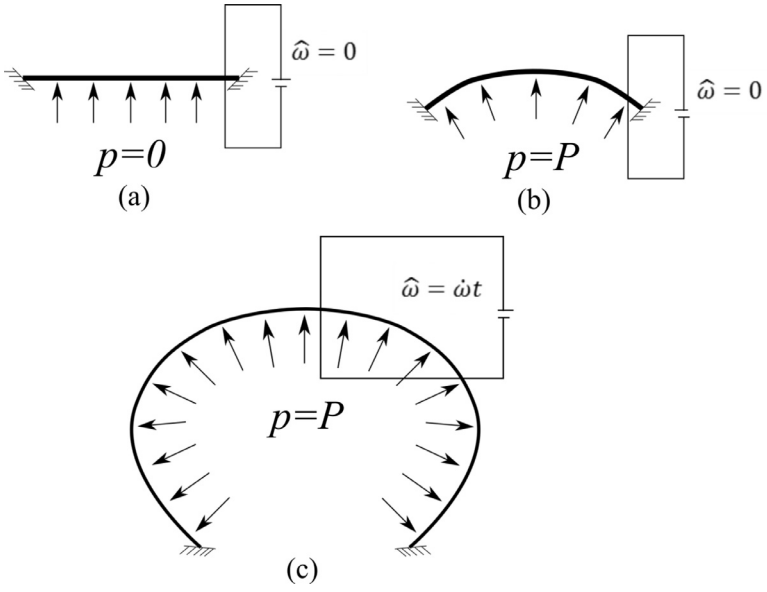


**Fig. 16. – Schematics of balloon inflation.**

numerical model is similar to the experiments in [53,54] (voltage control in experiments).

The profiles of membrane during inflation are illustrated in Fig. 17, together with the applied voltage vs balloon volume plot. After pre-inflation, the membrane slightly inflates, as in state (a), which is considered as the initial state. Then, the charge begins to ramp, and the membrane inflates inhomogeneously due to clamped edges until it is in state (b), where wrinkle occurs near the fixed boundary, and the voltage soon reaches the maximum value. At state (c), the wrinkle appears along the whole fixed edge, and electro-mechanical instability occurs, as discussed in the previous benchmark test. The calculation stops at state (d) because of the mesh distortion.

Observing the balloon profiles in the simulation results, the wrinkle behavior shown in Fig. 17(d) is similar to the experimental observation illustrated in Fig. 12 in [54], and Fig. 15 in [53]. A detailed analysis of the wrinkling phenomena is beyond the scope of the current paper, and will be conducted in future work.

## 5. Conclusion

In this work, we have proposed a hybrid element for DE simulation based on a four-field variational principle. The model is immune from volumetric locking, and capable of conducting coupled electromechanical analysis for an incompressible dielectric elastomer. The model is implemented using a C++ in-house code based on an open-source FEM library deal.II, and the source code is available to the community. Numerical tests show the capability and validity of such a model in simulating the electromechanical response for both static and dynamic

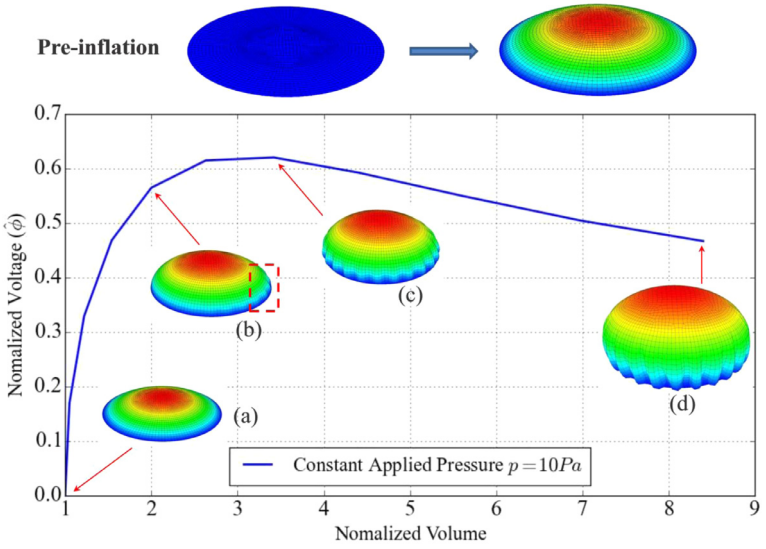


**Fig. 17. – The profile of balloon inflation at different stages.**

problems, as well as conducting eigenvalue analysis to investigate the vibration modes of a dielectric elastomer actuator. This model can be potentially used for design, analysis, development, and optimization of such soft active materials.

## Acknowledgment

The authors acknowledge the support under A*STAR SERC grant (132-183-0025).

## Appendix A. Tangent stiffness tensor in spatial configuration

The relationship of spatial and material tangent stiffness tensor is [43]:

$$\mathfrak{C}_{ijkl} = J^{-1}F_{iI}F_{jJ}F_{kK}F_{lL}\mathbb{C}_{IJKL} \tag{A.1}$$

where $\mathbb{C}_{IJKL}$ is the material tangent stiffness, while $\mathfrak{C}_{ijkl}$ represents its spatial counterpart.

We also have

$$\mathbb{C}_{IJKL} = 2\frac{\partial S_{IJ}}{\partial C_{KL}} = 2\left(\frac{\partial S_{IJ}^{\mathrm{dev}}}{\partial C_{KL}} + \frac{\partial S_{IJ}^{\mathrm{vol}}}{\partial C_{KL}} + \frac{\partial S_{IJ}^{\mathrm{ele}}}{\partial C_{KL}}\right). \tag{A.2}$$

Therefore, after derivation, the following spatial tangent stiffness tensor can be obtained.

The deviatoric part of the tensor:

$$\mathfrak{C}_{ijkl}^{\mathrm{dev}} = \frac{2\mu}{Ja}\left[\frac{1}{aJ_m}\bar{B}_{ij}\bar{B}_{kl} - -\left(\frac{\bar{I}_1}{3aJ_m} + \frac{1}{3}\right)\bar{B}_{ij}\delta_{kl} - -\left(\frac{\bar{I}_1}{3aJ_m} + \frac{1}{3}\right)\bar{B}_{kl}\delta_{ij} + \left(\frac{\bar{I}_1^2}{9aJ_m} + \frac{\bar{I}_1}{9}\right)\delta_{ij}\delta_{kl} + \frac{\bar{I}_1}{6}\left(\delta_{ik}\delta_{jl} + \delta_{il}\delta_{jk}\right)\right]. \tag{A.3}$$

The volumetric part of the tensor:

$$\mathfrak{C}_{ijkl}^{\mathrm{vol}} = \frac{K(1-J^2)}{2J}\left(\delta_{ik}\delta_{jl} + \delta_{il}\delta_{jk}\right) + KJ\delta_{ij}\delta_{kl}. \tag{A.4}$$

However, because of the imposing of independent pressure-like field, the modified volumetric part of tangent stiffness tensor now becomes

$$\mathfrak{C}_{ijkl}^{\mathrm{vol}} = -\tilde{p}\left(\delta_{ik}\delta_{jl} + \delta_{il}\delta_{jk} - \delta_{ij}\delta_{kl}\right) \tag{A.5}$$

The electric part of the tensor

$$\mathfrak{C}_{ijkl}^{\mathrm{ele}} = \frac{1}{2}\varepsilon(\delta_{ik}\delta_{jl} + \delta_{il}\delta_{jk} - \delta_{ij}\delta_{kl})E_aE_a + \varepsilon(\delta_{kl}E_iE_j + \delta_{ij}E_kE_l - \delta_{il}E_jE_k - \delta_{ik}E_jE_l - \delta_{jl}E_iE_k - \delta_{jk}E_iE_l). \tag{A.6}$$

## Appendix B. Open-source finite element program

The source code for our finite element program is available at: https://github.com/nicklj/de_implicit.git.

## Supplementary materials

Supplementary material associated with this article can be found, in the online version, at doi:10.1016/j.camss.2017.07.005.

REFERENCES

[1] R. Pelrine, R. Kornbluh, Q. Pei, J. Joseph, High-speed electrically actuated elastomers with strain greater than 100%, Science. 287 (2000) 836–839.
[2] J. Huang, S. Shian, Z. Suo, D.R. Clarke, Maximizing the energy density of dielectric elastomer generators using equi-biaxial loading, Adv. Funct. Mater 23 (2013) 5056–5061.
[3] C. Keplinger, J.-Y. Sun, C.C. Foo, P. Rothemund, G.M. Whitesides, Z. Suo, Stretchable, transparent, ionic conductors, Science 341 (2013) 984–987.

[4] H. Godaba, C.C. Foo, Z.Q. Zhang, B.C. Khoo, J. Zhu, Giant voltage-induced deformation of a dielectric elastomer under a constant pressure, Appl. Phys. Lett. 105 (2014) 112901.
[5] Z. Suo, Mechanics of stretchable electronics and soft machines, MRS Bull. 37 (2012) 218–225.
[6] I.A. Anderson, T.A. Gisby, T.G. McKay, B.M. O'Brien, E.P. Calius, Multi-functional dielectric elastomer artificial muscles for soft and smart machines, J. Appl. Phys. 112 (2012) 41101.
[7] M. Bozlar, C. Punckt, S. Korkut, J. Zhu, Dielectric elastomer actuators with elastomeric electrodes, Cit. Appl. Phys. Lett. 101 (2012) 91907.
[8] S. Shian, K. Bertoldi, D.R. Clarke, Dielectric elastomer based "Grippers" for soft robotics, Adv. Mater. 27 (2015) 6814–6819.
[9] J. Shintake, S. Rosset, B. Schubert, D. Floreano, H. Shea, Versatile soft grippers with intrinsic electroadhesion based on multifunctional polymer actuators, Adv. Mater. 28 (2016) 231–238.
[10] J.-Y. Sun, C. Keplinger, G.M. Whitesides, Z. Suo, Ionic skin, Adv. Mater. 26 (2014) 7608–7614.
[11] R.D. Kornbluh, R. Pelrine, H. Prahlad, A. Wong-Foy, B. McCoy, S. Kim, J. Eckerle, T. Low, From boots to buoys: promises and challenges of dielectric elastomer energy harvesting, Electroactivity in Polymeric Materials, Springer US, 2012, pp. 67–93.
[12] R. Kaltseis, C. Keplinger, S.J.A. Koh, R. Baumgartner, Y.F. Goh, W.H. Ng, A. Kogler, A. Tröls, C.C. Foo, Z. Suo, S. Bauer, Natural rubber for sustainable high-power electrical energy generation, RSC Adv. 4 (2014) 27905–27913.
[13] T. Li, S. Qu, W. Yang, Electromechanical and dynamic analyses of tunable dielectric elastomer resonator, Int. J. Solids Struct. 49 (2012) 3754–3761.
[14] B.-X. Xu, R. Mueller, A. Theis, M. Klassen, D. Gross, Dynamic analysis of dielectric elastomer actuators, Appl. Phys. Lett. 100 (2012) 112903.
[15] L. Liu, H. Chen, J. Sheng, J. Zhang, Experimental study on the dynamic response of in-plane deformation of dielectric elastomer under alternating electric load, Smart Mater. Struct. 23 (2014) 25037.
[16] J. Sheng, H. Chen, B. Li, Y. Wang, Nonlinear dynamic characteristics of a dielectric elastomer membrane undergoing in-plane deformation, Smart Mater. Struct. 23 (2014) 45010.
[17] U. Gupta, H. Godaba, Z. Zhao, C.K. Chui, J. Zhu, Tunable force/displacement of a vibration shaker driven by a dielectric elastomer actuator, Extrem. Mech. Lett. 2 (2015) 72–77.
[18] Z. Lu, H. Godaba, Y. Cui, C.C. Foo, M. Debiasi, J. Zhu, An electronically tunable duct silencer using dielectric elastomer actuators, J. Acoust. Soc. Am. 138 (2015) 236–241.
[19] J.W. Fox, N.C. Goulbourne, On the dynamic electromechanical loading of dielectric elastomer membranes, J. Mech. Phys. Solids. 56 (2008) 2669–2686.
[20] J. Zhu, S. Cai, Z. Suo, Resonant behavior of a membrane of a dielectric elastomer, Int. J. Solids Struct. 47 (2010) 3254–3262.
[21] P. Dubois, S. Rosset, M. Niklaus, M. Dadras, H. Shea, Voltage control of the resonance frequency of dielectric electroactive polymer (DEAP) membranes, J. Microelectromech. Syst. 17 (2008) 1072–1081.
[22] J. Zhu, S. Cai, Z. Suo, Nonlinear oscillation of a dielectric elastomer balloon, Polym. Int. 59 (2010) 378–383.
[23] J.W. Fox, N.C. Goulbourne, Electric field-induced surface transformations and experimental dynamic characteristics of dielectric elastomer membranes, J. Mech. Phys. Solids. 57 (2009) 1417–1435.
[24] K. Jia, T. Lu, T.J. Wang, Response time and dynamic range for a dielectric elastomer actuator, Sens. Actuators A Phys. 239 (2016) 8–17.
[25] Z. Suo, Theory of dielectric elastomers, Acta Mech. Solida Sin. 23 (2010) 549–578.
[26] X. Zhao, Z. Suo, Method to analyze programmable deformation of dielectric elastomer layers, Appl. Phys. Lett. 93 (2008) 251902.
[27] S. Qu, Z. Suo, A finite element method for dielectric elastomer transducers, Acta Mech. Solida Sin. 25 (2012) 459–466.
[28] C.C. Foo, Z.-Q. Zhang, A finite element method for inhomogeneous deformation of viscoelastic dielectric elastomers, Int. J. Appl. Mech. 7 (2015) 1550069.
[29] D.L. Henann, S.A. Chester, K. Bertoldi, Modeling of dielectric elastomers: design of actuators and energy harvesting devices, J. Mech. Phys. Solids. 61 (2013) 2047–2066.
[30] S. Wang, M. Decker, D.L. Henann, S.A. Chester, Modeling of dielectric viscoelastomers with application to electromechanical instabilities, J. Mech. Phys. Solids. 95 (2016) 213–229.
[31] J. Zhou, W. Hong, X. Zhao, Z. Zhang, Z. Suo, Propagation of instability in dielectric elastomers, Int. J. Solids Struct. 45 (2008) 3739–3750.
[32] Z.-Q. Zhang, C.C. Foo, G.R. Liu, A semi-explicit finite element method for dynamic analysis of dielectric elastomers, Int. J. Comput. Methods. 12 (2015) 1350108.
[33] H.S. Park, T.D. Nguyen, Viscoelastic effects on electromechanical instabilities in dielectric elastomers, Soft Matter. 9 (2013) 1031–1042.
[34] H.S. Park, Z. Suo, J. Zhou, P.A. Klein, A dynamic finite element method for inhomogeneous deformation and electromechanical instability of dielectric elastomer transducers, Int. J. Solids Struct. 49 (2012) 2187–2194.
[35] H.S. Park, Q. Wang, X. Zhao, P.A. Klein, Electromechanical instability on dielectric polymer surface: modeling and experiment, Comput. Methods Appl. Mech. Eng. 260 (2013) 40–49.
[36] S. Seifi, H.S. Park, Computational modeling of electro-elasto-capillary phenomena in dielectric elastomers, Int. J. Solids Struct. 87 (2016) 236–244.
[37] Tahoe, (2014) http://sourceforge.net/projects/tahoe/.
[38] T. Schlögl, S. Leyendecker, Electrostatic–viscoelastic finite element model of dielectric actuators, Comput. Methods Appl. Mech. Eng. 299 (2016) 421–439.
[39] W. Bangerth, D. Davydov, T. Heister, L. Heltai, G. Kanschat, M. Kronbichler, M. Maier, B. Turcksin, D. Wells, The deal.II Library, Version 8.4, J. Numer. Math. (2016) 135–141.
[40] R. Ortigosa, A.J. Gil, C.H. Lee, A computational framework for large strain nearly and truly incompressible electromechanics based on convex multi-variable strain energies, Comput. Methods Appl. Mech. Eng. 310 (2016) 297–334.
[41] J.C. Simo, R.L. Taylor, K.S. Pister, Variational and projection methods for the volume constraint in finite deformation elasto-plasticity, Comput. Methods Appl. Mech. Eng. 51 (1985) 177–208.
[42] A.N. Gent, A new constitutive relation for rubber, Rubber Chem. Technol 69 (1996) 59–61.
[43] G.A. Holzapfel, Nonlinear Solid Mechanics: A Continuum Approach for Engineering, John Wiley & Sons Ltd, 2000.
[44] T.J.R. Hughes, The Finite Element Method: Linear Static and Dynamic Finite Element Analysis, Dover Publications, 1987.
[45] X. Zhao, W. Hong, Z. Suo, Electromechanical hysteresis and coexistent states in dielectric elastomers, Phys. Rev. B Cond. Matter. 76 (2007) 134113.
[46] W. Frei, Improving convergence of multiphysics problems, (2013). https://www.comsol.com/blogs/improving-convergence-multiphysics-problems/.
[47] SIMULIA, Abaqus Analysis User's Guide V6.14, Section, SIMULIA, 2014 6.7.3.

[48] J. Reinders, Intel Threading Building Blocks, O'Reilly Media, Sebastopol, CA, 2007.
[49] T.A. Davis, Suitesparse: a suite of sparse matrix software, (2011). http://faculty.cse.tamu.edu/davis/suitesparse.html.
[50] Y.-K. Yong, Y. Cho, Numerical algorithms for solutions of large eigenvalue problems in piezoelectric resonators, Int. J. Numer. Meth. Engng. 39 (1996) 909–922.
[51] M. Heroux, Trilinos web page, (2016). https://trilinos.org/.
[52] W. Weaver, S.P. Timoshenko, D.H. Young, Vibration Problems in Engineering, John Wiley & Sons, 1990.
[53] T. Li, C. Keplinger, R. Baumgartner, S. Bauer, W. Yang, Z. Suo, Giant voltage-induced deformation in dielectric elastomers near the verge of snap-through instability, J. Mech. Phys. Solids. 61 (2013) 611–628.
[54] F. Wang, C. Yuan, T. Lu, T.J. Wang, Anomalous bulging behaviors of a dielectric elastomer balloon under internal pressure and electric actuation, J. Mech. Phys. Solids. 102 (2017) 1–16.